Available online at www.eccomasproceedia.org
Eccomas Proceedia COMPDYN (2023) 3893-3907

ECCOMAS
Proceedia

COMPDYN 2023
9th ECCOMAS Thematic Conference on
Computational Methods in Structural Dynamics and Earthquake Engineering
M. Papadrakakis, M. Fragiadakis (eds.)
Athens, Greece, 12-14 June 2023

ON THE CALIBRATION OF UBCSAND CONSTITUTIVE MODEL AGAINST MONOTONIC & CYCLIC TRIAXIAL COMPRESSION DATA FOR BALLAST AGGREGATES

Tadahiro Kishida[1], **Rusul F. Aldulaimi**[1] **and George Mylonakis**[1]

[1] Khalifa University
UAE
{tadahiro.kishida, 100059665, george.mylonakis}@ku.ac.ae

Abstract

Understanding the mechanical behavior of ballast aggregates under multi-axial loading is key in railway foundation analysis and design. UBCSAND is an effective-stress constitutive model which can predict static and dynamic behavior of granular materials under combined shear and normal stresses. This study presents results from a suite of triaxial monotonic and cyclic compression tests for four different aggregates (gabbro, limestone, demolished concrete, steel slag) and discusses the applicability of UBCSAND model for simulating the relevant non-linear stress-strain curves. To this end, UBCSAND is integrated, for the first time, analytically for shear and volumetric strains, to facilitate calibration against experimental data. Four novel solutions are derived, expressed in terms of monomials and Gauss' hypergeometric functions ($_2F_1$) of the stress ratio (q/p'). Variation in the calibrated parameters is discussed considering different loading conditions and types of aggregates.

Keywords: UBCSAND, drained & undrained triaxial tests, analytical solution, numerical calibration

ISSN:2623-3347
Peer-review under responsibility of the organizing committee of COMPDYN 2023.
doi: 10.7712/120123.10688.21357

1 INTRODUCTION

Understanding drained monotonic and cyclic behavior of ballast aggregates is key in railway foundation design. The UBCSAND model [1-3] is often employed in such analyses, as a simple alternative to more complex constitutive formulations for predicting monotonic and cyclic response of granular soil under both drained and undrained conditions [4-23]. The specific model is employed in commercial finite difference and finite element software (e.g., [3, 24-26]) as it realistically simulates volumetric and deviatoric strains in granular soils under monotonic and cyclic loading.

The study at hand presents an analytical methodology for integrating the UBCSAND model that yields a set of four novel closed-form solutions for shear and volumetric strains. Contrary to numerical integration approaches, these solutions are free of numerical errors and, thereby, can provide insight on the role of the various model parameters and their calibration against experimental data. Three novel methodologies developed by the authors in a companion paper [27] for calibrating the model are compared: (1) a graphical "chart" solution based on results from forward numerical simulations; (2) a numerical approach based on minimization of residuals; (3) a trial-and-error graphical approach based on the analytical solution. These calibration procedures are applied to experimental data from drained strain- and stress-controlled triaxial compression tests carried out in the Geotechnical Materials Lab at Khalifa University on four types of aggregates: gabbro, limestone, demolished concrete and steel slag. The performance of the model with number of cycles is discussed against data from cyclic compression tests.

2 UBCSAND FORMULATION

The pressure-dependent, non-linear elastic shear and bulk moduli (G^e, K^e) can be established by means of Eqs. (1) and (2), as functions of the mean effective stress p' and Poisson's ratio ν [30]

$$G^e = k_G^e \left(\frac{p'_M}{p_a}\right)^{ne} p_a \tag{1}$$

$$K^e = \frac{2(1+\nu)}{3(1-2\nu)} G^e \tag{2}$$

where k_G^e is a dimensionless elastic shear modulus parameter, p_a is the atmospheric pressure (usually taken equal to 100 kPa) and $p'_M = (\sigma'_1 + \sigma'_3)/2$ is the familiar MIT mean effective stress. In Eq. (1), the elastic shear modulus exponent *ne* is often taken equal to around 0.5 based on experimental observations of small-strain shear moduli (e.g., [31-33]).

The incremental elastic stress-strain relation can be cast in terms of G^e and K^e as shown in Eq. (3).

$$\begin{bmatrix} dp' \\ dq \end{bmatrix} = \begin{bmatrix} K^e & 0 \\ 0 & 2G^e \end{bmatrix} \begin{bmatrix} d\varepsilon_v^e \\ d\gamma^e \end{bmatrix} \tag{3}$$

where p' and q are the corresponding Cambridge stress invariants defined as $p' = (\sigma'_1 + \sigma'_2 + \sigma'_3)/3$, $q = \sigma'_1 - \sigma'_3$ under triaxial loading, and $d\varepsilon_v^e$, $d\gamma^e$ are the corresponding incremental volumetric and shear strains $d\varepsilon_v^e = d\varepsilon_a^e + 2d\varepsilon_r^e$, $d\gamma^e = d\varepsilon_a^e - d\varepsilon_r^e$. Since UBCSAND employs the MIT stress path parameters $p'_M = \frac{1}{2}(\sigma'_1 + \sigma'_3)$ and $q_M = \frac{1}{2}(\sigma'_1 - \sigma'_3)$, Equation (3) can be recast in the following equivalent forms:

$$\begin{bmatrix} dp'_M \\ dq_M \end{bmatrix} = \begin{bmatrix} K^e & G^e/3 \\ 0 & G^e \end{bmatrix} \begin{bmatrix} d\varepsilon_v^e \\ d\gamma^e \end{bmatrix} \tag{4a}$$

$$\begin{bmatrix} d\varepsilon_v^e \\ d\gamma^e \end{bmatrix} = \begin{bmatrix} 1/K^e & -1/3K^e \\ 0 & 1/G^e \end{bmatrix} \begin{bmatrix} dp'_M \\ dq_M \end{bmatrix} \tag{4b}$$

With reference to elastoplastic response, the yield surface is defined as

$$f = \eta - \eta_{mob} = 0 \tag{5}$$

where $\eta = q_M/p'_M$ is the dimensionless stress ratio. Yielding occurs when η reaches the mobilized stress ratio η_{mob}.

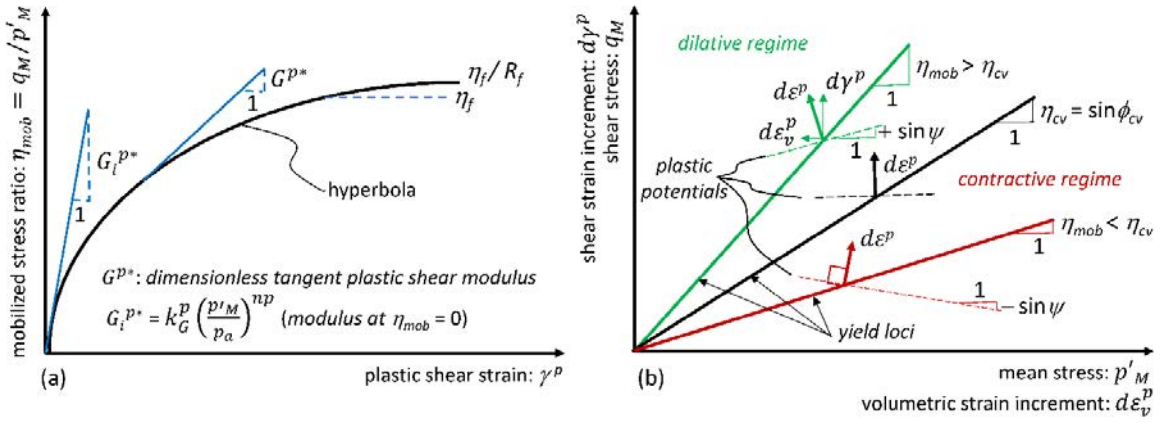

Figure 1. (a) Hardening rule; (b) Yield criterion and flow rule for UBCSAND model [27]

The hardening rule can be expressed in differential form using the total derivative:

$$d\gamma^p = \frac{1}{G^{p*}} d\eta_{mob} = \frac{1}{G^{p*} p'_M} \left(-\eta_{mob} dp'_M + dq_M\right) \tag{6}$$

where G^{p*} is a dimensionless plastic shear modulus relating $d\gamma^p$ and $d\eta$. In the realm of the specific model, G^{p*} is estimated from the empirical relation

$$G^{p*} = k_G^p \left(\frac{p'_M}{p_a}\right)^{np} \left(1 - \frac{\eta_{mob}}{\eta_f / R_f}\right)^2 \tag{7}$$

where k_G^p is a dimensionless plastic shear modulus parameter (being equal to G^{p*}at $p'_M = p_a$ and $\eta_{mob} = 0$), and η_f is the stress ratio at failure. R_f is the failure ratio adjustment for preventing the over-prediction of strength at failure [2, 34]. The plastic shear modulus exponent *np* is usually selected in the range 0.4 – 0.7 [29].

The flow rule is of the non-associative type and is given by the simple equation

$$\frac{d\varepsilon_v^p}{d\gamma^p} = \eta_{cv} - \eta_{mob} \tag{8}$$

where η_{cv} is the stress ratio under constant volume. A graphical illustration of the UBCSAND hardening and flow rules, mathematically expressed by Eqs. (6) and (8) respectively, is provided in Figure 1.

By combining Eqs. (6) and (8), the plastic strain increment can be expressed as

$$\begin{bmatrix} d\varepsilon_v^p \\ d\gamma^p \end{bmatrix} = \frac{1}{G^{p*} p'_M} \begin{bmatrix} -\eta_{mob}(\eta_{cv} - \eta_{mob}) & \eta_{cv} - \eta_{mob} \\ -\eta_{mob} & 1 \end{bmatrix} \begin{bmatrix} dp'_M \\ dq_M \end{bmatrix} \tag{9}$$

Adding Eqs. (4b) and (9), the combined elastic and plastic volumetric and shear strain increments are obtained from the equation:

$$\begin{bmatrix} d\varepsilon_v \\ d\gamma \end{bmatrix} = \begin{bmatrix} C_{11} & C_{12} \\ C_{21} & C_{22} \end{bmatrix} \begin{bmatrix} dp'_M \\ dq_M \end{bmatrix} \tag{10}$$

where

$$C_{11} = \frac{1}{K^e} + \frac{-\eta_{mob}(\eta_{cv} - \eta_{mob})}{G^{p*} p'_M} \qquad C_{12} = \frac{-1}{3K^e} + \frac{\eta_{cv} - \eta_{mob}}{G^{p*} p'_M} \tag{11a,b}$$

$$C_{21} = \frac{-\eta_{mob}}{G^{p*} p'_M} \qquad C_{22} = \frac{1}{G^e} + \frac{1}{G^{p*} p'_M} \tag{11c, d}$$

are the elements of the compliance matrix $\boldsymbol{C}$. Explicit formulae obtained upon substituting Eq. (7) into Eqs (11) are provided in [27].

The stress increments are obtained from the stiffness formulation in Eq. (12):

$$\begin{bmatrix} dp'_M \\ dq_M \end{bmatrix} = \begin{bmatrix} D_{11} & D_{12} \\ D_{21} & D_{22} \end{bmatrix} \begin{bmatrix} d\varepsilon_v \\ d\gamma \end{bmatrix} \tag{12}$$

where D_{11}, D_{12}, D_{21} and D_{22} are the elements of the stiffness matrix $\boldsymbol{D}$ (inverse of matrix $\boldsymbol{C}$ in Eq. (10)). Explicit formulae obtained by substituting Eqs. (1) and (7) into Eqs (12) are provided in [27]. For stress-controlled drained triaxial compression $\delta q_M = \delta p'_M$; the overall volumetric strain increment can then be obtained from $d\gamma$ as follows:

$$d\varepsilon_v = \left(\frac{D_{22} - D_{12}}{D_{11} - D_{21}}\right) d\gamma \tag{13}$$

The initial shear modulus (G_o) of isotropically consolidated samples under triaxial drained compression ($dq_M = dp'$) can be obtained from the terms C_{21} and C_{22} in Eq. (10) as $G_o = dq_M/d\gamma = 1/(C_{21} + C_{22})$. This yields the following solution

$$G_o = \frac{k_G^e k_G^p}{k_G^p \left(\frac{p'_M}{p_a}\right)^{1-n^e} + k_G^e \left(\frac{p'_M}{p_a}\right)^{-n^p}} p'_M \tag{14}$$

where p_M' (= p_c') is the isotropic confining stress. Evidently, since η_{mob} is assumed equal to 0, there is no purely elastic regime so that elastic and plastic strains coexist even at zero deviatoric stress. Accordingly, a combination of parameters k_G^e and k_G^p control the value of G_o. Setting $\eta_{mob} = 0^+$ allows for an elastic region in the limit sense, prohibiting plastic deformations ($k_G^P \rightarrow +\infty$). Imposing this condition to Eq. (14) yields the anticipated result $G_o = G^e$ according to Eq. (1).

3. ANALYTICAL INTEGRATION

The UBCSAND hardening and flow rule differential in Eqs. (6) and (8) can be integrated analytically for different stress paths. Considering triaxial compression and drained conditions, the mean effective stress can be expressed as $p'_M = p'_c + q_M$, where p'_c is the effective confining pressure at zero deviatoric stress. As the stress ratio η is equal to q_M/p'_M, the mean effective stress and the deviatoric stress at the plane of loading can be expressed as functions of η via the equations:

$$p'_M = \frac{1}{1-\eta} p'_c \tag{15}$$

$$q_M = \frac{\eta}{1-\eta} p'_c \tag{16}$$

Combining Eq. (16) with Eqs. (1) and (4b), and after some trivial algebraic manipulations, the elastic shear strain increment can be expressed as

$$d\gamma^e = \frac{dq_M}{G^e} = \frac{1}{k_G^e(1-\eta)^{2-ne}} \left(\frac{p'_c}{p_a}\right)^{1-ne} d\eta \tag{17}$$

Integrating the above equation over η yields the elastic shear strain in closed form

$$\gamma^e = \frac{-1}{k_G^e\ (1-ne)} \left[1 - \frac{1}{(1-\eta)^{1-ne}}\right] \left(\frac{p'_c}{p_a}\right)^{1-ne} \tag{18}$$

expressed as a function of five dimensionless parameters (k_G^e, η, ν, ne and p'_c/p_a).

In the same vein, using Eq. (15) and Eq. (7), Eq. (6) can be expressed in terms of η to give the plastic shear strain increment

$$d\gamma^p = \frac{1}{k_G^p \left(\frac{p'_c}{p_a}\right)^{np} \left(1-\frac{\eta}{\eta_f/R_f}\right)^2} (1-\eta)^{np} d\eta \tag{19}$$

The above equation can be integrated analytically for the plastic shear strain

$$\gamma^p = \frac{1}{k_G^p \left(\frac{p'_c}{p_a}\right)^{np} (1-np)} \left[\frac{(1-\eta)^{(1+np)}}{\left(1-\frac{\eta}{\eta_f/R_f}\right)^2} \ {}_2F_1\left[1,2,2-np, \frac{1-\frac{1}{\eta_f/R_f}}{1-\frac{\eta}{\eta_f/R_f}}\right] - \ {}_2F_1\left[1,2,2-np, 1-\frac{1}{\eta_f/R_f}\right] \right] \tag{20}$$

where ${}_2F_1$ is the Gaussian hypergeometric function [35]. The elastic volumetric strain can be obtained in a similar manner as the elastic shear strain, by combining Eqs. (15) and (16) with Eq. (4b) to get

$$d\varepsilon_v^e = \frac{dp'_M}{K^e} - \frac{dq_M}{3K^e} = \frac{2p'_c}{3K^e(1-\eta)^2} d\eta \tag{21}$$

Substituting Eqs. (1) and (2) in the above formula and integrating over η yields

$$\varepsilon_v^e = \int_0^\eta \frac{1}{k_G^e(1-\eta)^{2-ne}} \frac{(1-2\nu)}{(1+\nu)} \left(\frac{p'_c}{p_a}\right)^{1-ne} d\eta = \frac{-1}{k_G^e\ (1-ne)} \left[1 - \frac{1}{(1-\eta)^{1-ne}}\right] \frac{(1-2\nu)}{(1+\nu)} \left(\frac{p'_c}{p_a}\right)^{1-ne} \tag{22}$$

which is a function of the same dimensionless parameters as γ^e in Eq. (18).

Finally, the plastic volumetric strain can be derived analytically from the flow rule. Indeed, substituting Eq. (19) in Eq. (8) and integrating with respect to η, one gets

$$\varepsilon_v^p = \int_0^\eta \frac{a(1-\eta)^{np}(\eta_{cv}-\eta)}{k_G^p \left(\frac{p'_c}{p_a}\right)^{np} \left(1-\frac{\eta}{\eta_f/R_f}\right)^2} d\eta \tag{23}$$

where a is a fitting parameter typically taken equal to 1. The solution to the above integral is

$$\varepsilon_v^p = \frac{a\ \eta_f/R_f}{k_G^P \left(\frac{p'_c}{p_a}\right)^{np}} (X_1 - X_2 - X_3) \tag{24}$$

where,

$$X_1 = -\frac{\left(1-\frac{\eta_{cv}}{\eta_f/R_f}\right)}{\left(1-\frac{1}{\eta_f/R_f}\right)}\left\{1-\left[1+\frac{\left(1-\frac{1}{\eta_f/R_f}\right)}{np\left(1-\frac{\eta_{cv}}{\eta_f/R_f}\right)}\right]{}_2F_1\left[1,1,1-np,1-\frac{1}{\eta_f/R_f}\right]\right\} \quad (25a)$$

$$X_2 = -\frac{\eta_f/R_f{}^{(1+np)}\left(1-\frac{\eta_{cv}}{\eta_f/R_f}\right)}{(1-np)\left(1-\frac{\eta}{\eta_f/R_f}\right)^{1-np}}\ {}_2F_1\left[1-np,-np,2-np,\frac{\left(1-\frac{1}{\eta_f/R_f}\right)}{\left(1-\frac{\eta}{\eta_f/R_f}\right)}\right] \quad (25b)$$

$$X_3 = -\frac{\eta_f/R_f{}^{(1+np)}}{np\left(1-\frac{\eta}{\eta_f/R_f}\right)^{-np}}\ {}_2F_1\left[-np,-np,1-np,\frac{\left(1-\frac{1}{\eta_f/R_f}\right)}{\left(1-\frac{\eta}{\eta_f/R_f}\right)}\right] \quad (25c)$$

are dimensionless functions. Like in the solution in Eq. (20), no general conclusions can be gleaned as to the behavior of functions X_1, X_2, X_3 without numerical evaluation of the series. A graphical illustration of Eqs. (25) is provided in [27]. The above analysis can be readily extended to other stress paths (such as triaxial extension), but this lies beyond the scope of this work.

As a final remark, integrating over η implies a monotonic increase of η from zero (or a finite value). This stress-controlled loading implies no η-softening with the analytical approximation. To account for such softening (which is a common trait of the response of dense sands under drained loading), modifications in the analysis would be required which lie beyond the scope of this work.

4. PARAMETER SELECTION

The dimensionless parameters involved in the model are: k_G^p, k_G^e, η_f/R_f, η_{cv}, ν, ne and np. The last three, ν, ne and np, are often selected empirically and for the purposes of these study we have assumed $\nu = 0.2$, $ne = 0.5$, $np = 0.4$ based on the following brief discussion.

The elastic Poisson's ratio ν is typically selected between 0 to 0.2 [2, 30] based on studies of small strain elastic response of sands [36]. Recent laboratory experiments have confirmed that ν ranges from 0.1 to 0.3 for different granular materials [37-38]. In this light, the value $\nu \approx 0.2$ seems reasonable.

In the ensuing, np has been taken equal to 0.4 based on the tested materials and stress conditions.

5. APPLICATION TO DRAINED MONOTONIC & CYCLIC TESTS

5.1 Test Materials

The experiments carried out in the Geotechnical Materials Lab at Khalifa University involved four different materials: (a) gabbro; (b) limestone; (c) demolished concrete; and (d) electric arc furnace (EAF) slag. Gabbro is a coarse grain igneous rock that is rich in iron, magnesium and calcium, and is extracted at the border between UAE and Oman. It is both strong and suitable for construction. Limestone is a sedimentary rock made of calcium carbonate, and is available throughout the UAE. It is weaker than gabbro, but also suitable for construction and provides excellent drainage when used as ballast. Demolished concrete is a recycled material - a mixture of cement and aggregates. The cement is weak and crushable. More than 29 million tons of cement are produced annually in the UAE [39]. Slag is a by-product of smelting

generated as industrial waste during steel-making process. Slag is stronger and more resilient than the other three materials. More than 800,000 tons of slag are annually produced in the UAE [40].

Gabbro and demolished concrete particles are rounded, whereas limestone and slag have sharp angular shapes. Table 1 presents a summary of the grain-size distribution and their characteristics. All materials show uniform gradations. The effective grain size (D_{10}) ranges from 4.6 to 12.8 mm, whereas the coefficient of uniformity (C_u) ranges from 1.3 to 1.7.

Table 1. Summary of tested materials [27]

Material	*D_{10} (mm)*	*C_u*	*Particle shape*	*Mineralogy*
Gabbro	9.7	1.3	Sub-rounded	Coarse-grained silicate
Limestone	4.6	1.7	Angular	Calcium carbonate
Demolished concrete	6.7	1.4	Sub-rounded	Calcium carbonate, silicate aggregate
EAF Slag	12.8	1.3	Sub-angular	Calcium and iron oxide

5.2 Test Procedure

Triaxial tests were conducted using a GCTS Testing System device (Model No.: SSC-2K-0000). Details are provided in [27] The tests were conducted in three stages:

Stage 1) Isotropic consolidation under confining stress $\sigma'_c = 50\ kPa$.

Stage 2) Drained cyclic loading with $q_M = 50\ kPa$ with a loading frequency of 1 *Hz*. The applied number of cycles (N) varied from 50 to 200.

Stage 3) Triaxial compression under drained conditions.

5.3 Experimental Drained Cyclic and Monotonic Compression Measurements

Figure 2 shows the cyclic loading responses between q_M and axial strain (ε_a) for each material from 1 to 50 cycles. The gabbro testing displayed stiff behavior, whereas slag demonstrated ratcheting. The residual ε_a and volumetric strain (ε_v) against N, is presented in Figures 3(a) and (b). ε_a and ε_v gradually increase with N, where the slag and the gabbro show the largest and smallest strains, respectively. Limestone and demolished concrete exhibit an intermediate behavior. The accumulation of ε_a and ε_v is similar indicating that the radial strain is limited during cyclic compression. This observation is consistent with previous studies [41], where the radial strain was limited when the amplitude of cyclic load is less than 70% of the static peak strength. In fact, the amplitude of cyclic q_M (Figure 2) applied in this study was approximately 40% of the static peak strength (Figure 14). Figure 14(a) shows a drained monotonic compression response in terms of deviatoric shear stress q_M versus shear strain γ. Limestone exhibits the highest strength (~160 kPa), whereas the other three materials have similar strengths in the range 120-150 kPa. Figure 14(b) plots ε_v versus γ. The largest and smallest dilatancies were observed in gabbro and demolished concrete, respectively.

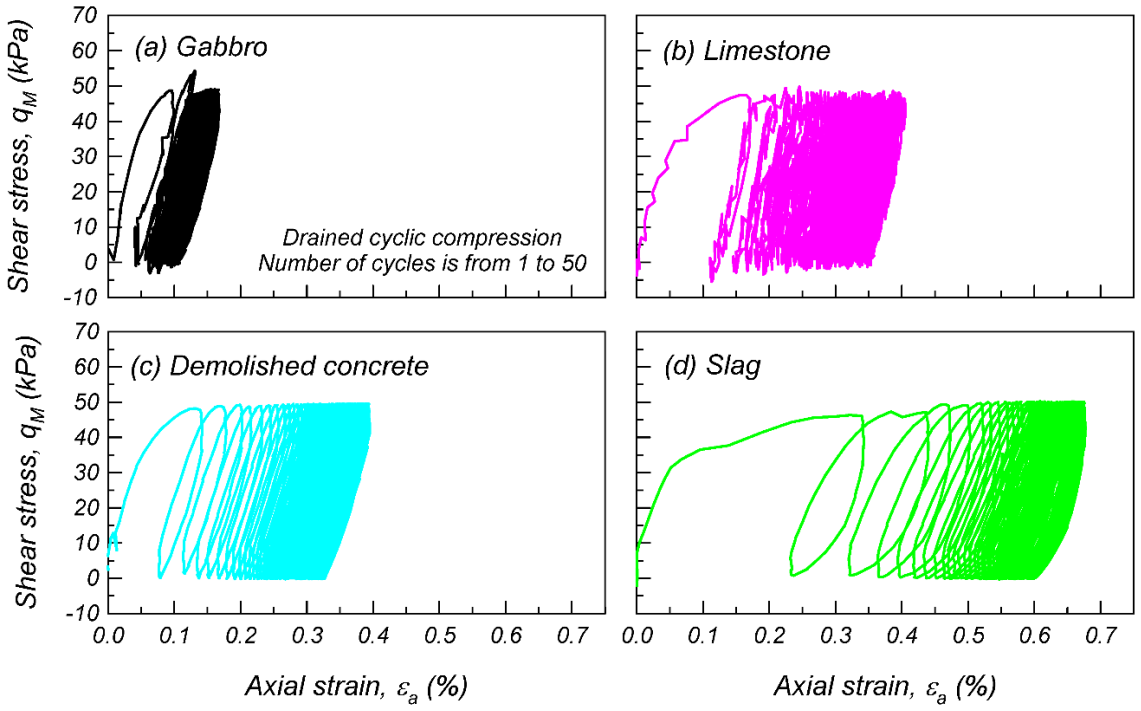

Figure 2. Drained cyclic compression test results: (a) Gabbro, (b) Limestone, (c) Demolished concrete, (d) Slag. In all tests σ'_c = 50 kPa, q_M = 50 kPa [27].

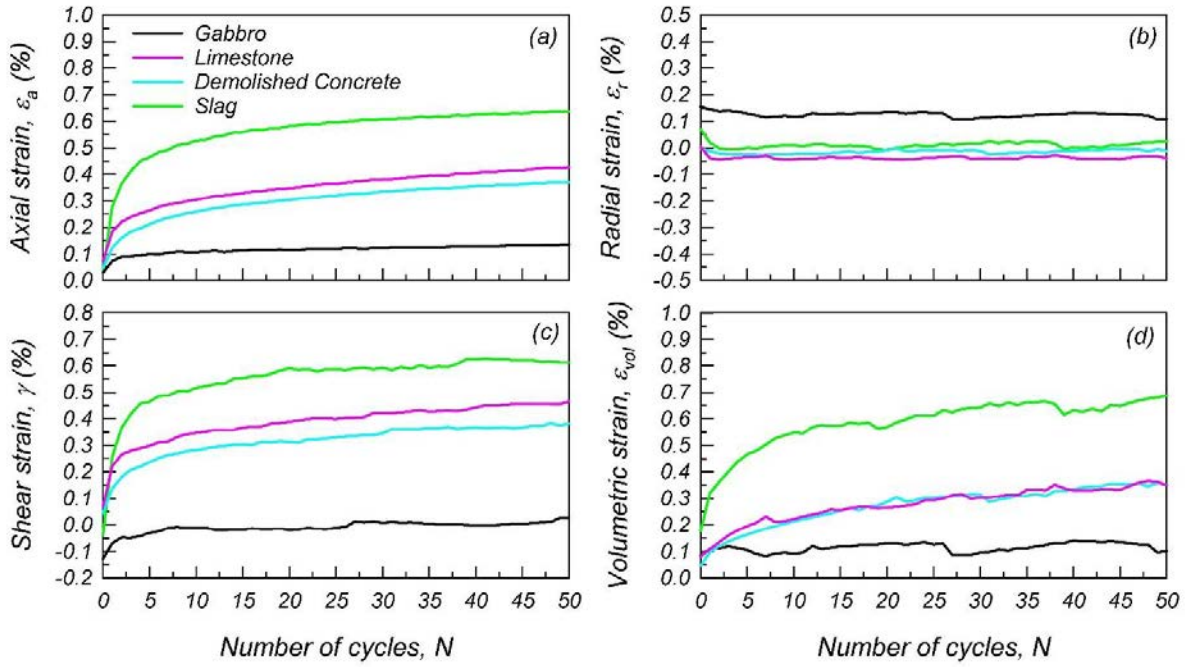

Figure 3. Cyclic drained compression test results for different materials: (a) ε_a vs. N, (b) ε_r vs. N (d) γ vs. N. In all tests σ'_c = 50 kPa, q_M = 50 kPa [27].

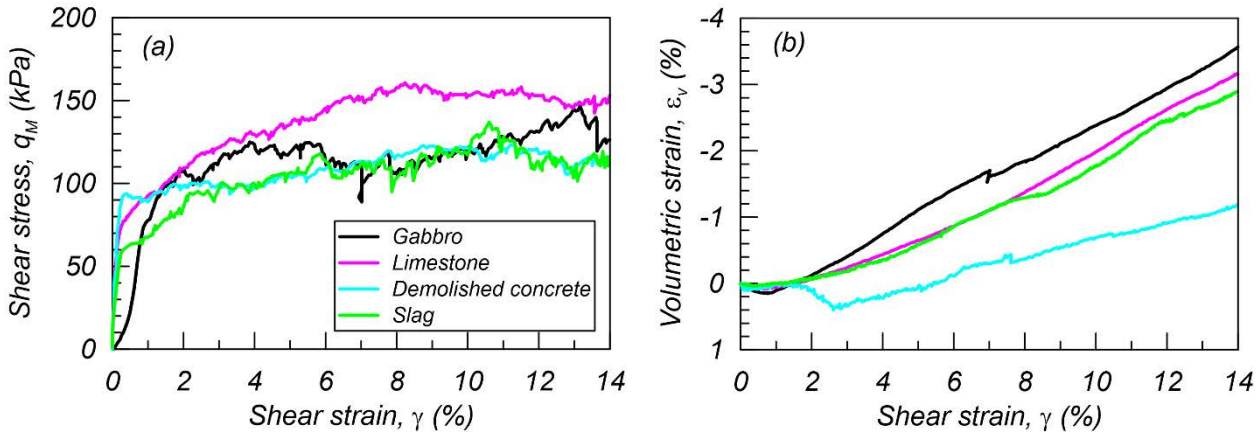

Figure 4. Monotonic drained compression test results for different materials (a) q_M vs. γ (b) ε_v vs. γ [27].

5.4 Calibration of UBCSAND Model to the Experimental Data

UBCSAND models were calibrated both numerically and analytically using the aforementioned experimental data from drained monotonic compression tests. The numerical and graphical 'chart' solutions for strain-controlled conditions follow the procedures described in detail in [27]. Table 2 provides UBCSAND parameters estimated by employing the three different calibration approaches presented in this study: analytical, chart solution, numerical. Figure 5(a)-(h) presents the calibrated responses of η vs. γ and ε_v vs. γ computed following these approaches. It is demonstrated that the main aspects of the drained monotonic compression response are reproduced adequately by all three methods relative to the experimental data in Figure 4. The analytical and numerical solutions work best for strains above 1% while the chart solution deviates from both and from the experimental data as well, except for strains less than 1%.

Table 2. Calibrated UBCSAND parameters against drained monotonic triaxial compression data for four different ballast aggregates using the three methods described in this paper (σ'_c = 50 kPa) [27].

Material	Method	k_G^p	k_G^p/k_G^e	η_f/R_f	η_{cv}
Gabbro	Analytical	500	2.00	0.75	0.42
	Chart	234	2.00	0.73	0.36
	Numerical	620	2.77	0.74	0.41
Limestone	Analytical	400	0.10	0.77	0.50
	Chart	720	0.02	0.77	0.53
	Numerical	410	0.10	0.77	0.50
Demolished concrete	Analytical	1000	0.10	0.70	0.60
	Chart	1,640	0.02	0.71	0.55
	Numerical	980	0.05	0.68	0.59
EAF Slag	Analytical	300	0.50	0.68	0.42
	Chart	700	0.02	0.68	0.53
	Numerical	320	0.05	0.68	0.44

ne, *np*, and *v* values are fixed at 0.5, 0.4, and 0.2, respectively.

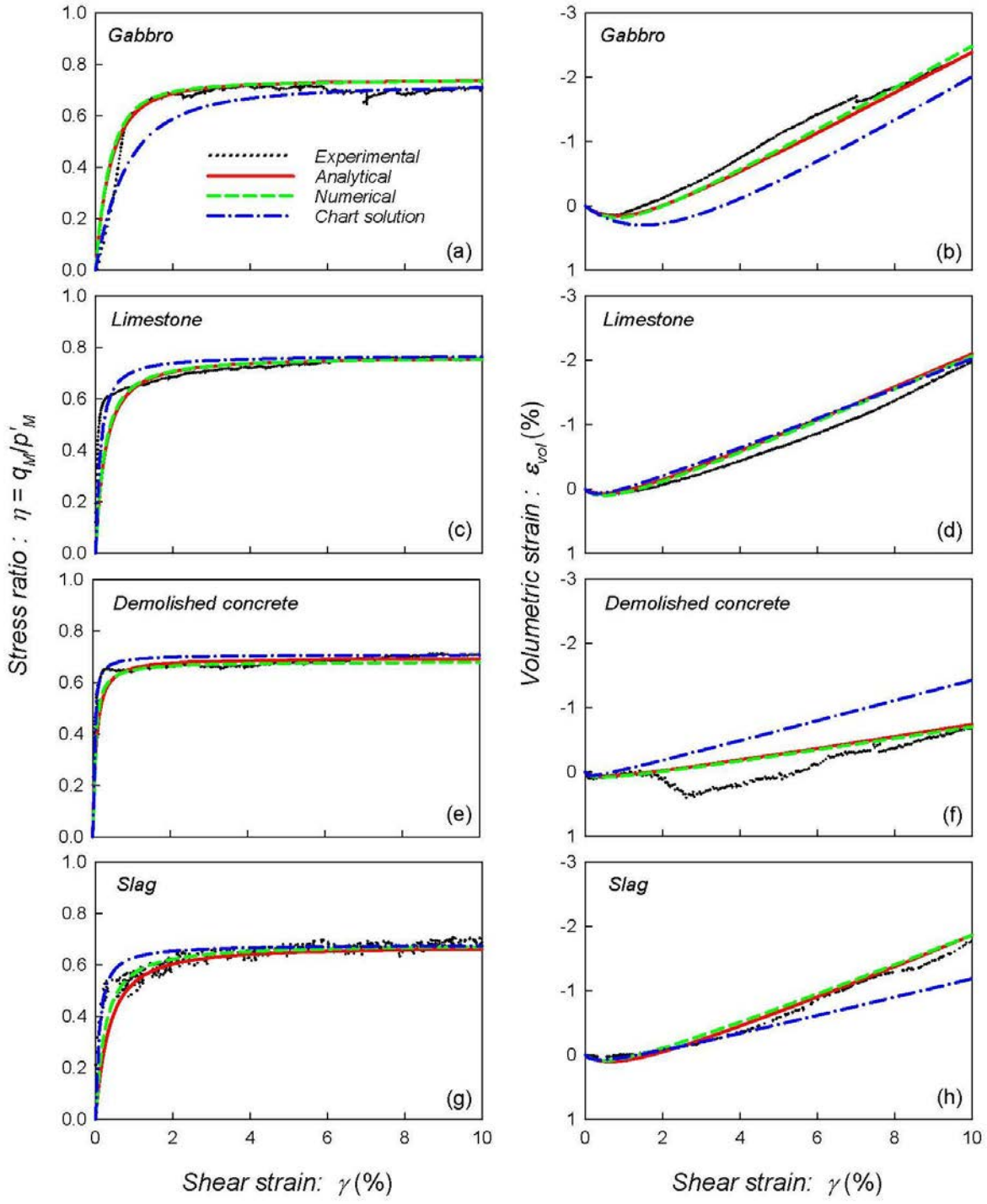

Figure 5. Calibrated monotonic drained compression tests for four different aggregate materials using the analytical, numerical and chart solutions. The UBCSAND parameters for each case are provided in Table 3. (a) η vs. γ, (b) ε_v vs. γ for gabbro, (c) η vs. γ, (d) ε_v vs. γ for limestone, (e) η vs. γ, (f) ε_v vs. γ for demolished concrete, (g) η vs. γ, (h) ε_v vs. γ for slag [27].

Figure 6 shows the example responses of UBCSAND for drained cyclic compression tests of gabbro and slag, using the parameters of numerical calibration in Table 2. The slag simulation exhibits the largest residual ε_a compared to gabbro, which is consistent with the experimental observations in Figure 2. However, the rate of strain accumulation is constant for UBCSAND, which is different from the experimental findings. Figure 7 shows the residual

values of ε_a and ε_v for drained cyclic compression computed with UBCSAND using the parameters in Table 2. Comparing the results from Figures 3 and 7, it is fair to mention that the model parameters should be different for cyclic versus monotonic loading, which complicates its application for combinations of static and dynamic loads (a most common case in earthquake engineering).

Moreover, the rate of increase of volumetric and shear strains with number of cycles is linear, hence cannot realistically reproduce results for excess pore pressures under undrained loading. This is evident in Fig. 8 where different calibrations are needed for different number of cycles. These observations are important when trying to apply the specific model to dynamic problems – notably for soil liquefaction analysis.

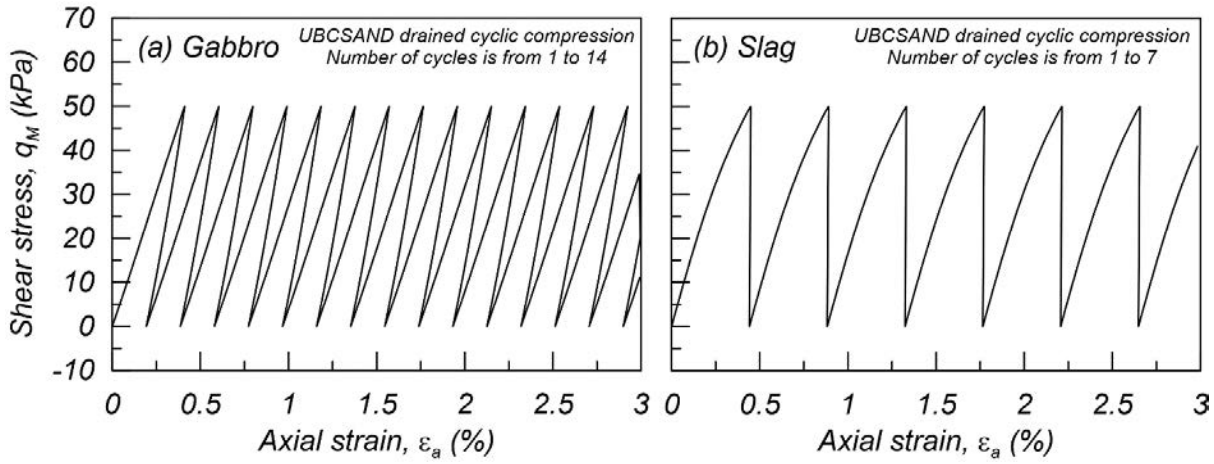

Figure 6. Example of q_M vs. ε_a cyclic drained response predicted using UBCSAND model based on the calibrated parameters in Table 3: (a) gabbro, (b) slag [27].

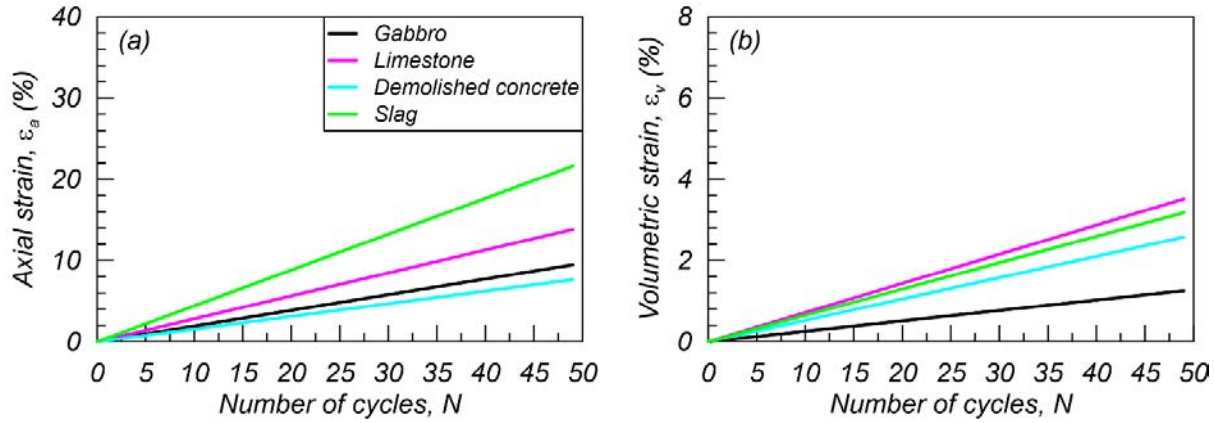

Figure 7. Examples of residual axial and volumetric strains predicted using UBCSAND for drained cyclic compression using the calibrated parameters in Table 2: (a) ε_a vs. N; (b) ε_v vs. N (σ'_c = 50 kPa, q_M = 50 kPa) [27].

The UBCSAND model was calibrated against drained cyclic compression tests for different number of loading cycles. Table 3 shows the calibrated parameters for N from 0 to 2, 0 to 10 and 0 to 50 cycles for different materials, respectively. The calibration procedure follows Figure 8 for stress-controlled conditions. The parameters k_G^p/k_G^e and η_f/R_f are fixed from Table 2 for drained monotonic conditions. The k_G^p/k_G^e ratio was fixed because the calibrated value was very large (i.e. small k_G^e) due to the plastic deformations developing during successive unloading cycles. η_f/R_f was fixed because it does not provide a reliable value due to the

low amplitude of cyclic loads to determine the failure parameters. Table 3 shows that the k_G^p parameter increases as the number of cycles increases. η_{cv} similarly increases as the number of cycles increases when the material exhibits contractive behavior.

Figure 8 shows the residual strains ε_a and ε_v for slag under drained cyclic tests compared with the calibrated UBCSAND for different loading conditions. The results suggest that the UBCSAND model can be reasonably fitted by adjusting the calibration range. The figure also shows that the calibrated parameters against drained monotonic compression tests only predict the cyclic compression responses well when N is not larger than 1 - 4 cycles. Evidently, there is no single set of parameters which can reproduce well both drained monotonic and cyclic conditions.

Table 3. Numerically calibrated UBCSAND parameters against drained cyclic compression tests (σ'_c = 50 kPa, q_M = 100 kPa) [27].

Material	# of cycles N	k_G^p	k_G^p/k_G^e	η_f/R_f	η_{cv}
Gabbro	0 – 2	5,400	2.77	0.74	0.61
	0 – 10	18,500	2.77	0.74	0.32
	0 - 50	69,600	2.77	0.74	0.36
Limestone	0 – 2	1,500	0.10	0.77	0.54
	0 – 10	4,800	0.10	0.77	0.74
	0 - 50	15,900	0.10	0.77	0.86
Demolished concrete	0 – 2	2,900	0.05	0.68	1.00
	0 – 10	7,700	0.05	0.68	1.00
	0 - 50	25,300	0.05	0.68	0.99
EAF Slag	0 – 2	760	0.05	0.68	0.50
	0 – 10	2,800	0.05	0.68	0.71
	0 - 50	11,900	0.05	0.68	0.83

ne, *np*, and *v* values are fixed at 0.5, 0.4, and 0.2, respectively. k_G^p/k_G^e and η_f/R_f values are fixed based on the monotonic compression tests

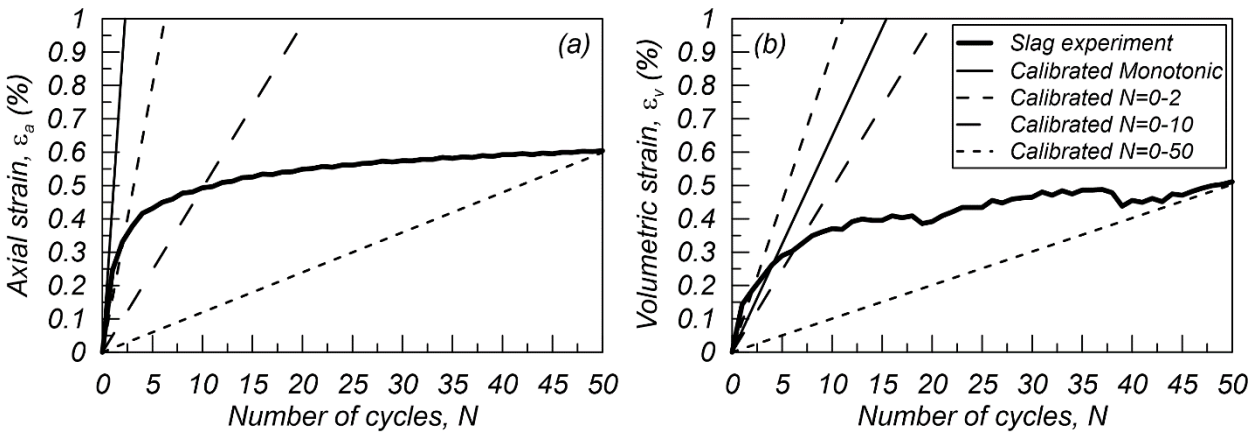

Figure 8. Comparison of residual strains of slag between experimental and UBCSAND models calibrated based on different loading conditions: (a) N vs. ε_a, (b) N vs. ε_v; σ'_c = 50 kPa, q_M = 50 kPa [27].

6. CONCLUSIONS

The popular UBCSAND constitutive model was reviewed and integrated analytically for monotonic and cyclic drained triaxial compression conditions. A novel closed form solution for the elastic and plastic shear and volumetric strains was presented. Three new methodologies for calibrating the model parameters to experimental data were compared: (1) a graphical "chart" solution; (2) a numerical approach based on minimization of residuals; and (3) a trial-and-error approach based on the analytical solution. It has been demonstrated that:

(1) The analytical solution provides an excellent tool, free of numerical errors, for calibrating the UBCSAND parameters against laboratory data.
(2) Results from the numerical calibration against both monotonic and cyclic test data show that the parameters of UBCSAND are different between monotonic and cyclic drained compression conditions. The calibrated parameters against monotonic tests only predict the cyclic compression responses well when N is less than 1 - 4 cycles. Therefore, UBCSAND models should be calibrated against the target loading conditions and number of cycles.
(3) The model parameters should be different for cyclic versus monotonic loading, which makes its application for combinations of static and dynamic loads (a most common case in earthquake engineering) difficult.
(4) The rate of increase of volumetric and shear strains with number of cycles is always linear, hence cannot realistically reproduce results for excess pore pressures under undrained loading.

These observations are important when trying to apply the specific model to dynamic problems – notably in soil liquefaction analysis.

7. ACKNOWLEDGEMENTS

The work presented in this paper was funded by the Khalifa University of Science & Technology – Competitive Internal Research Award CIRA 2019-015 [Project Title: "SUPERTRACK: Superior Performance Railway TRACKS for the UAE"] and FSU 2021-028 [Project Title: "Next Generation Framework for Seismic Design of Quay Walls"]. The third author is supported by Khalifa University Combined Master's/Doctoral Research/Teaching Scholarship (CMDRTS). The authors are grateful to Saif Bin Darwish Crusher, Mawaad Environmental Services, Star International Waste Management LLC, and Al Dhafra Recycling Industries for providing the testing materials used in this study.

8. REFERENCES

[1] Beaty, M.H., Byrne, P.M. (1998). An effective stress model for predicting liquefaction behaviour of sand. *Geotechnical Earthquake Engineering and Soil Dynamics III ASCE Geotechnical Special Publication*, **75**(1):766-777.
[2] Beaty, M.H., Byrne, P.M. (2011). UBCSAND constitutive model: Version 904aR. *Documentation Report: UBCSAND Constitutive Model on Itasca UDM Web Site*; February 2011. http://www.itasca-udm.com/pages/UBCSand.html.
[3] Tsegaye, A. (2010). PLAXIS liquefaction model. *Report no. 1. PLAXIS knowledge base*.
[4] Schofield, A.N., Wroth P. (1968). *Critical State Soil Mechanics*. McGraw-Hill Book Company
[5] Prévost, J.H., Hoeg. K. (1975). Effective Stress-Strain-Strength Model for Soils. *Journal of Geotechnical Engineering-ASCE*. **101** (GT3, Proc. Paper 11157): 259-278.
[6] Nova, R., Wood, D.M. (1979). A constitutive model for sand in triaxial compression. *International journal for numerical and analytical methods in geomechanics.* **3**(3):255-278
[7] Manzari, M. T., Dafalias, Y. F. (1997). A critical state two-surface plasticity model for sands. *Géotechnique,* 47:2, 255-272. https://doi.org/10.1680/geot.1997.47.2.255

[8] Jefferies, M.G. (1993) Nor – Sand: a simple critical state model for sand. *Géotechnique*, **43**(1): 91-103
[9] Pestana, J. M., Whittle, A. J. (1995). Compression Model for Cohesionless Soils. *Géotechnique*, **45**(4): 611-631. doi:10.1680/geot.1995.45.4.611
[10] Papadimitriou, A.G. & Bouckovalas, G. (2002). Plasticity model for sand under small and large cyclic strains: A multiaxial formulation. *Soil Dyn. Earthquake Eng*., **22** (3): 191-204, 10.1016/S0267-7261(02)00009-X
[11] Been, K., Jefferies, M.G. (2004). Stress-dilatancy in very loose sand. *Canadian Geotechnical Journal.* **41**: 972-989. doi: 10.1139/T04-038
[12] Loukidis, D. and Salgado, R. (2009). Modeling sand response using two-surface plasticity. *Comput. Geotech.*, **36** (1–2):166-186, 10.1016/j.compgeo.2008.02.009
[13] Karamitros, D.K. (2010) *Development of a numerica:l algorithm for the dynamic elastoplastic analysis of geotechnical structures in two and three dimensions.* PhD Thesis, Dept of Civil Engineering, NTUA, Athens
[14] Diambra, A., Ibraim, E., Russell, A.R., Wood, D.M. (2013). Fibre reinforced sands: from experiments to modelling and beyond. *International Journal for Numerical and Analytical Methods in Geomechanics*. **37**(15): 2427-2455.
[15] Boulanger, R.W., Ziotopoulou K. (2015). PM4Sand (Version 3): A sand plasticity model for earthquake engineering applications. *Report No. UCD/CGM-15/01, Center for Geotechnical Modeling Department of Civil and Environmental Engineering University of California Davis*.
[16] Cubrinovski, M., Ishihara, K. (1998). State Concept and Modified Elastoplasticity for Sand Modelling, *Soils and Foundations*, **38**(4): 213-225
[17] Hashiguchi, K., Mase, T., Yamakawa, Y. (2021). Elaborated subloading surface model for accurate description of cyclic mobility in granular materials, *Acta Geotechnica,* 17:699–719, https://doi.org/10.1007/s11440-021-01203-y
[18] Yang, M., Seidalinov, G., Taiebat, M. (2019). Multidirectional cyclic shearing of clays and sands: Evaluation of two bounding surface plasticity models, *Soil Dynamics and Earthquake Engineering*, 124: 230-258
[19] Barrero, A. R., Taiebat, M., Dafalias, Y. F. (2020). Modeling cyclic shearing of sands in the semifluidized state, *Int J Numer Anal Methods Geomech*; 44:371–388
[20] Yang, M., Taiebat, M. and Dafalias, Y. F. (2020). SANISAND-MSf: a sand plasticity model with memory surface and semifluidised state, *Géotechnique,* https://doi.org/10.1680/jgeot.19.P.363
[21] Duque, J., Yang, M., Fuentes, W., Mas, D., Taiebat, M. (2021). Characteristic limitations of advanced plasticity and hypoplasticity models for cyclic loading of sands, *Acta Geotechnica*, https://doi.org/10.1007/s11440-021-01418-z
[22] Asaoka, A. Noda, T., Yamada, E., Kaneda, K. and Nakano, M. (2002). An Elasto-Plastic Description of Two Distinct Volume Change Mechanisms of Soils, *Soils and Foundations*. **42**(5): 47-57.
[23] Corti, R., Diambra, A., Wood, D. M., Escribano, D. E., Nash, D. F. T. (2016). Memory Surface Hardening Model for Granular Soils under Repeated Loading Conditions, *J. Eng. Mech*., **142**(12): 04016102.
[24] Itasca (2011). FLAC, Fast Lagrangian Analysis of Continua, Version 7.0. Itasca Consulting Group, Minneapolis, MN; 2011. http://www.itascacg.com/.
[25] Shriro, M., Bray, J.D. (2013). Calibration of numerical model for liquefaction-induced effects on levees and embankments. *Seventh International Conference on Case Histories in Geotechnical Engineering.* 29 April – 3 May, Chicago
[26] PLAXIS (2018). Computer aided geotechnical analysis software. Bentley Systems, https://www.bentley.com/en/products/brands/plaxis.
[27] Voyagaki E., Kishida T., Aldulaimi R.F., Mylonakis G. (2023). Integration and calibration of UBCSAND model for drained monotonic and cyclic triaxial compression of aggregates, *Soil Dynamics & Earthquake Engineering.* 171 107978, https://doi.org/10.1016/j.soildyn.2023.107978

[28] Puebla, H., Byrne, P.M., Phillips, R. (1997). Analysis of CANLEX liquefaction embankments: Prototype and centrifuge models. *Canadian Geotechnical Journal*, **34**: 641–657.
[29] Petalas, A., Galavi, V. (2013). PLAXIS Liquefaction Model UBC3D-PLM. Available online: https://communities.bentley.com/cfs-file/__key/communityserver-wikis-components-files/00-00-00-05-58/UBC3D_2D00_PLM_2D00_REPORT.June2013.pdf.
[30] Beaty, M.H. (2018). Application of UBCSAND to the LEAP centrifuge experiments. *Soil Dynamics and Earthquake Engineering*, **104**: 143-153.
[31] Seed and Idriss. (1970). Soil Moduli and Damping Factors for Dynamic Response Analyses. *Report EERC70-10, Earthquake Engineering Research Center*, University of California, Berkeley.
[32] Hardin, B.O., Drnevich, V.P. (1972). Shear modulus and damping in soils: Design equations and curves. *Journal of the Soil Mechanics and Foundations Division, ASCE*. SM7: 667-692
[33] Darendeli, M.B. (2001). *Development of a new family of normalized modulus reduction and material damping curves.* PhD Thesis. The University of Texas at Austin
[34] Duncan, J.M., Chang, C.Y. (1970). Nonlinear analysis of stress and strain in soils. *Journal of the Soil Mechanics and Foundations Division, ASCE*, **96**(5): 1629-1653.
[35] Abramowitz, M., Stegun, I. (1970). *Handbook of Mathematical Functions with Formulas*. Graphs, and Mathematical Tables, Dover Publications, ISBN: 0486612724.
[36] Hardin, B.O. (1978). The Nature of Stress-Strain Behaviour for Soils. *Proceedings of Earthquake Engineering and Soil Dynamics, ASCE*, Pasadena, 19-21 June 1978, 3-89.
[37] Hoque, E. & Tatsuoka, F. (1998). Anisotropy in Elastic Deformation of Granular Materials, *Soils and Foundations*. **38** (1): 163-179.
[38] Suwal, L. P. & Kuwano, R. (2018). Statically and Dynamically Measured Poisson's Ratio of Granular Soils on Triaxial Laboratory Specimens, *Geotechnical Testing Journal*, **36**(4): 493-505.
[39] Global Cement. (2015). *The growing cement industry of the UAE*. https://www.globalcement.com/magazine/articles/917-the-growing-cement-industry-of-the-uae. (Last accessed, November 2022)
[40] Emirates Steel. (2022). *Emirates Steel signs slag management agreement with Finnish company ECOFER Technologies – Emirates Steel*.
https://www.emiratessteelarkan.com/press/emirates-steel-signs-slag-management-agreement-with-finnish-company-ecofer-technologies/. (last accessed November 2022)
[41] Sun, Q.D., Indraratna, B., Nimbalkar, S. (2016). Deformation and Degradation Mechanisms of Railway Ballast under High Frequency Cyclic Loading. *Journal of Geotechnical & Geoenvironmental Engineering*, **142**(1): 04015056.